Accepted Manuscript

A stabilised immersed framework on hierarchical b-spline grids for fluid-flexible structure interaction with solid–solid contact

C. Kadapa, W. G. Dettmer, D. Perić

PII: S0045-7825(18)30102-6
DOI: https://doi.org/10.1016/j.cma.2018.02.021
Reference: CMA 11796

To appear in: *Comput. Methods Appl. Mech. Engrg.*

Received date : 27 October 2017
Revised date : 7 January 2018
Accepted date : 23 February 2018

Please cite this article as: C. Kadapa, W.G. Dettmer, D. Perić, A stabilised immersed framework on hierarchical b-spline grids for fluid-flexible structure interaction with solid–solid contact, *Comput. Methods Appl. Mech. Engrg.* (2018), https://doi.org/10.1016/j.cma.2018.02.021

Highlights (for review)

- A novel numerical scheme for the interaction of incompressible fluid, flexible solids and solid-solid contact.
- Immersed boundary methodology on hierarchical b-spline grids to deal with large solid displacements and topological changes.
- Mixed Galerkin formulation with SUPG/PSPG stabilisation for incompressible fluid flow.
- Second-order accurate time integration schemes along with second-order accurate staggered solution scheme.
- A simple mapping technique for uncovering fluid degrees of freedom.

A stabilised immersed framework on hierarchical b-spline grids for fluid-flexible structure interaction with solid-solid contact

C. Kadapa*, W. G. Dettmer, D. Perić

Zienkiewicz Centre for Computational Engineering, College of Engineering, Swansea University, Fabian Way, Swansea SA1 8EN, Wales, UK.

Abstract

We present a robust and efficient stabilised immersed framework for fluid-structure interaction involving incompressible fluid flow and flexible structures undergoing large deformations and also involving solid-solid contact. The efficiency of the formulation stems from the use of second-order accurate sequential staggered solution scheme for resolving fluid-solid coupling. Mixed Galerkin formulation, along with SUPG/PSPG stabilisation, is employed to obtain the numerical solutions of the incompressible Navier-Stokes equations. The immersed formulation is based on hierarchical b-spline grids, with unsymmetric Nitsche method employed to impose boundary as well as interface conditions on the fluid domain, while ghost-penalty operators are applied to alleviate the numerical instabilities arising due to small cut cells. The solid is modelled using linear continuum elements with finite strain formulation to facilitate the modelling of large structural deformations, and the contact between solids is modelled using the normal frictionless node-to-segment contact elements with Lagrange multipliers. In order to deal with the issue of uncovering for cut-cell based numerical schemes, a simple mapping technique is also introduced. Spatial and temporal convergence studies of the proposed scheme are performed by studying a simple example of flow over a deformable beam in cross flow. The robustness and accuracy of the proposed scheme are demonstrated by studying the benchmark examples of an oscillating beam in two-dimensions and flutter of a flexible simplified bridge deck in three-dimensions. In order to demonstrate the applicability of the proposed framework to complex fluid-structure interaction problems, the proposed methodology is used to simulate the fluid-structure interaction of a check valve with flexible valve plate.

Keywords: Fluid-structure interaction; Hierarchical b-splines; Immersed boundary methods; Staggered scheme; Nitsche method; Check valve.

1. Introduction

Computer simulation of complex fluid-structure interaction is a challenging task due to numerous difficulties associated with geometrical and physical characteristics of this multi-physics phenomenon. The foremost challenges are: (a) complexity of the geometry of the structure, (b) large structural deformations, (c) topological changes in

*Corresponding author
Email address: c.kadapa@swansea.ac.uk (C. Kadapa)

the fluid domain, (d) added-mass instabilities, and (e) achieving robustness and efficiency. A considerable amount of research and development has been done addressing some of these difficulties to a reasonable extent, and some numerical schemes are available in commercial software tools. However, many of the issues, for example, effectively dealing with complex geometries and topological changes and staggered schemes with higher-order accuracies, are still open and require to be addressed successfully in order for the efficient simulation of complex fluid-structure interaction problems.

Despite their academic success and availability in commercial software tools, numerical schemes based on the well-established arbitrary Lagrangian-Eulerian (ALE) formulation using body-fitted meshes, see [1–7] and references therein, are not an ideal choice for simulating complex FSI problems where the structures undergo extremely large deformations, with possible topological changes of simulation domain. The unavoidable requirement for re-meshing techniques to solve complex FSI problems makes body-fitted based FSI schemes inefficient and, therefore, limits their applicability. To overcome these difficulties and to model complex FSI effectively and efficiently, numerical schemes based on immersed/embedded strategies are becoming the obvious alternatives.

In general, in the immersed boundary methods, the fluid is modelled in the Eulerian frame of reference while the solid is described in the Lagrangian frame of reference. In these family of methods, the fluid grid does not have to align with the fluid-solid interface. Therefore, the cumbersome process of generating body-fitted meshes and complex re-meshing algorithms for dealing with large-structural deformations is completely avoided. However, because of the fact that the fluid mesh does not align with the boundary of the solid, specialised techniques need to be employed in order to enforce interface conditions on the fluid domain and to transfer the force between the fluid and solid domains. Motivated by the pioneering work of Peskin [8], a variety of numerical schemes for FSI based on immersed/embedded strategies have been proposed, see [9–16].

With the aim of addressing the difficulties associated with modelling complex FSI, our recent research efforts have been focused on staggered solution schemes [6], isogeometric analysis [17, 18] and immersed boundary methods [19–21]. Inspired by the recent CutFEM approach by Burman et al. [22], a preliminary study of our immersed computational framework has been presented in Dettmer et al. [20], while its application to fluid-rigid body interaction is presented in Kadapa et al. [21]. The present article is focussed on the application of this immersed framework to fluid-flexible solid interaction.

The proposed computational framework is characterised by the following ingredients:

- The fluid problem is solved over a Cartesian grid discretised with b-splines. The hierarchical nature of b-splines is exploited for generating computationally efficient grids with localised refinements in the vicinity of the immersed solids.
- The solution of the fluid problem is obtained using mixed Galerkin formulation in combination with the well-established SUPG/PSPG stabilisation [23–25].
- The interface conditions, as well as boundary conditions on the fluid domain, are enforced using unsymmetric

Nitsche method.

- Edge-based ghost-penalty operators [26] are applied in order to overcome the instabilities due to small cut cells.
- Integration of cut cells is carried out using either sub-triangulation or adaptive integration, depending upon the requirement.
- Solids are discretised with linear quadrilateral elements with finite-strain Fbar formulation [27]. Therefore, the boundary of a solid is approximated using straight edges. It is important to point out that this is not a limitation of the present framework; linear elements are chosen only for the sake of simplicity. The framework can be easily extended to include solid geometries represented with higher-order elements, for example, NURBS, or parametric equations.
- Solid-solid contact is assumed to be frictionless and modelled using node-to-segment contact elements with Lagrange multipliers to impose the contact constraint.
- Second-order accurate generalised-α schemes are used for the time integration of both the fluid and solid problems, and a second-order accurate staggered scheme is employed for resolving the fluid-solid coupling. Thus, the overall methodology is based on the *second-order* accurate time integration procedures. As the fluid and solid subproblems are *solved only once* during each time step, the use of a second-order accurate staggered solution scheme makes the overall FSI formulation computationally very efficient.

The outline of the article is as follows. In Section 2, we present a brief overview of the finite element formulation. The coupling strategy, the staggered scheme, the aspects of force transfer and a mapping technique introduced to deal with the issue of uncovering are discussed in Section 3. Finally, the accuracy and the robustness of the proposed scheme are demonstrated using several numerical examples in Section 4. The summary and the conclusions are provided in Section 5.

2. Formulation

2.1. Governing equations

2.1.1. Governing equations for the fluid problem

In the present work, the fluid is assumed to be laminar, viscous and incompressible. The corresponding Navier-Stokes equations are given as,

$$\rho^f \frac{\partial \mathbf{v}^f}{\partial t} + \rho^f (\mathbf{v}^f \cdot \nabla)\mathbf{v}^f - \nabla \cdot \boldsymbol{\sigma}^f = \mathbf{g}^f \qquad \text{in} \quad \Omega^f \tag{1a}$$

$$\nabla \cdot \mathbf{v}^f = 0 \qquad \text{in} \quad \Omega^f \tag{1b}$$

$$\mathbf{v}^f = \bar{\mathbf{v}}^f \qquad \text{on} \quad \Gamma^f_{\mathrm{D}} \tag{1c}$$

$$\boldsymbol{\sigma}^f \cdot \mathbf{n}^f = \bar{\mathbf{t}}^f \qquad \text{on} \quad \Gamma^f_{\mathrm{N}}\,, \tag{1d}$$

where, ρ^f is the density of the fluid, $\mathbf{g}^f$ is the body force on the fluid domain, $\mathbf{v}^f$ as the velocity of the fluid, $\boldsymbol{\sigma}^f (= \mu^f \left[\nabla \mathbf{v}^f + (\nabla \mathbf{v}^f)^T\right] - p\,\mathbf{I})$ is the Cauchy stress tensor, μ^f is the dynamic viscosity of the fluid, p is the fluid pressure, $\mathbf{n}^f$ is the unit outward normal on the boundary Γ^f of the fluid domain Ω^f. $\bar{\mathbf{v}}^f$ and $\bar{\mathbf{t}}^f$ are the prescribed velocity and traction boundary conditions, respectively, on the Dirichlet boundary Γ^f_{D} and the Neumann boundary Γ^f_{N}. Here, $\Gamma^f_{\mathrm{D}} \bigcup \Gamma^f_{\mathrm{N}} = \Gamma^f$ and $\Gamma^f_{\mathrm{D}} \bigcap \Gamma^f_{\mathrm{N}} = \emptyset$.

2.1.2. Governing equations for the solid problem

Governing equations for the elastic solids are given as,

$$\rho^s \frac{\partial^2 \mathbf{d}^s}{\partial t^2} - \nabla \cdot \boldsymbol{\sigma}^s = \mathbf{g}^s \qquad \text{in} \quad \Omega^s \tag{2}$$

$$\mathbf{d}^s = \bar{\mathbf{d}}^s \qquad \text{on} \quad \Gamma^s_{\mathrm{D}} \tag{3}$$

$$\boldsymbol{\sigma}^s \cdot \mathbf{n}^s = \bar{\mathbf{t}}^s \qquad \text{on} \quad \Gamma^s_{\mathrm{N}}\,, \tag{4}$$

where, ρ^s is the density of solid, $\mathbf{d}^s$ is the displacement of the solid, $\boldsymbol{\sigma}^s$ is the Cauchy stress tensor, $\mathbf{g}^s$ is the body force acting on the solid domain, $\mathbf{n}^s$ is the unit outward normal on the boundary Γ^s of the solid domain Ω^s. $\bar{\mathbf{d}}^s$ and $\bar{\mathbf{t}}^s$ are the displacement and traction boundary conditions prescribed, respectively, on the Dirichlet boundary Γ^s_{D} and the Neumann boundary Γ^s_{N}. Here, $\Gamma^s_{\mathrm{D}} \bigcup \Gamma^s_{\mathrm{N}} = \Gamma^s$ and $\Gamma^s_{\mathrm{D}} \bigcap \Gamma^s_{\mathrm{N}} = \emptyset$.

The Cauchy stress tensor depends upon the type of material model considered for the solid. In this work, we have used two material models, namely Saint Venant-Kirchhoff and compressible Neo-Hookean, depending upon the requirements in the numerical examples considered. With deformation gradient $\mathbf{F}$, its determinant J, right Cauchy-Green deformation tensor $\mathbf{C}$, left Cauchy-Green deformation tensor $\mathbf{b}$, Lagrangian strain tensor $\mathbf{E}$, first Piola-Kirchhoff stress tensor $\mathbf{P}$ and second Piola-Kirchhoff stress tensor $\mathbf{S}$, the strain energy functions Ψ for Saint Venant-Kirchhoff and Neo-Hooken material models are given respectively as,

Saint Venant-Kirchhoff model:.

$$\Psi = \frac{1}{2}\lambda^s (\mathrm{tr}\mathbf{E})^2 + \mu^s \mathbf{E} : \mathbf{E} \tag{5}$$

Neo-Hookean model:.

$$\Psi = \frac{\mu^s}{2}(\mathrm{tr}\mathbf{b} - 3) - \mu^s \ln J + \frac{\lambda}{4}(J^2 - 1) - \frac{\lambda}{2}\ln J \tag{6}$$

where,

$$\mu^s = \frac{E^s}{2(1+\nu^s)} \quad \text{and} \quad \lambda^s = \frac{E^s \nu^s}{(1+\nu^s)(1-2\nu^s)} \tag{7}$$

are Lamé's constants, and E^s and ν^s are the Young's modulus and Poisson's ratio, respectively.

2.1.3. Interface constraints

At the interface Γ^{f-s} between fluid and solid, two important conditions have to be satisfied. The first condition is called the kinematic constraint, and it requires that the fluid-solid interface moves at the same velocity as that of the boundary of the solid. The second condition requires the equilibrium of stresses along the interface. These two interface conditions, in the absence of surface forces, can be written as,

$$\text{Kinematic constraint:} \qquad \mathbf{v}^f = \mathbf{v}^s \quad \text{on} \quad \Gamma^{f-s} \tag{8a}$$

$$\text{Stress equilibrium:} \qquad \boldsymbol{\sigma}^f \cdot \mathbf{n}^f + \boldsymbol{\sigma}^s \cdot \mathbf{n}^s = \mathbf{0} \quad \text{on} \quad \Gamma^{f-s} \tag{8b}$$

2.2. Integration in time

In the present work, we use the generalised-α schemes for time integration of both the fluid and solid problems. These time integration techniques are identical to the ones used for the fluid-rigid body interaction presented in Kadapa et al. [21]. Therefore, we refer to [21], and references therein, for the detailed discussion of these time integration schemes.

2.3. Finite element formulation for the fluid problem

The stabilised formulation for the fluid considered in the present work has been established in [20, 21]. Therefore, we outline only the important aspects of the formulation, and refer the reader to [20, 21] for an in-depth discussion.

Numerical solutions of the fluid problem are obtained by employing mixed Galerkin formulation along with SUPG/PSPG stabilisation, Nitsche's method for imposing Dirichlet boundary conditions as well as interface conditions on the fluid grid and ghost-penalty operators for alleviating the numerical instabilities arising due to small cut cells. The complete variational statement for the fluid problem reads as follows: find the fluid velocity $\mathbf{v}^f \in \mathcal{S}_\mathbf{v}$ and the pressure $p \in \mathcal{S}_p$ such that for all functions $\mathbf{w}^f \in \mathcal{V}_\mathbf{v}$ and $q \in \mathcal{V}_p$,

$$\begin{aligned} B^f_{\text{Gal}}(\{\mathbf{w}^f, q\}, \{\mathbf{v}^f, p\}) + B^f_{\text{Stab}}(\{\mathbf{w}^f, q\}, \{\mathbf{v}^f, p\}) + B^f_{\text{Nitsche}}(\{\mathbf{w}^f, q\}, \{\mathbf{v}^f, p\}) \\ + B^f_{\text{GP}}(\{\mathbf{w}^f, q\}, \{\mathbf{v}^f, p\}) = F^f_{\text{Gal}}(\{\mathbf{w}^f, q\}) \,, \end{aligned} \tag{9}$$

where $\mathcal{S}_\mathbf{v}, \mathcal{S}_p, \mathcal{V}_\mathbf{v}$ and $\mathcal{V}_p$ represent the appropriate b-spline approximation spaces. The expressions $B^f_{\text{Gal}}(\{\mathbf{w}^f, q\}, \{\mathbf{v}^f, p\})$ and $F^f_{\text{Gal}}(\{\mathbf{w}^f, q\})$ consist of terms corresponding to the standard Galerkin formulation while $B^f_{\text{Stab}}(\{\mathbf{w}^f, q\}, \{\mathbf{v}^f, p\})$, $B^f_{\text{Nitsche}}(\{\mathbf{w}^f, q\}, \{\mathbf{v}^f, p\})$, and $B^f_{\text{GP}}(\{\mathbf{w}^f, q\}, \{\mathbf{v}^f, p\})$ are, respectively, the terms corresponding to the SUPG/PSPG stabilisation, the Nitsche's method and the ghost penalty operators.

2.3.1. Standard Galerkin terms

The terms corresponding to the standard Galerkin formulation are given as

$$B^f_{\text{Gal}}(\{\mathbf{w}^f, q\}, \{\mathbf{v}^f, p\}) = \int_{\Omega^f} \mathbf{w}^f \cdot \rho^f \left(\frac{\partial \mathbf{v}^f}{\partial t} + \mathbf{v}^f \cdot \nabla \mathbf{v}^f \right) d\Omega^f + \int_{\Omega^f} \mu \, \nabla \mathbf{w}^f : \left[\nabla \mathbf{v}^f + (\nabla \mathbf{v}^f)^T \right] d\Omega^f - \int_{\Omega^f} \nabla \cdot \mathbf{w}^f \, p \, d\Omega^f + \int_{\Omega^f} q \, \nabla \cdot \mathbf{v}^f \, d\Omega^f \tag{10}$$

$$F^f_{\text{Gal}}(\{\mathbf{w}^f, q\}) = \int_{\Omega^f} \mathbf{w}^f \cdot \mathbf{g}^f \, d\Omega^f + \int_{\Gamma^f_{\text{N}}} \mathbf{w}^f \cdot \bar{\mathbf{t}}^f \, d\Gamma \, . \tag{11}$$

2.3.2. SUPG/PSPG stabilisation

The terms corresponding to SUPG/PSPG formulation are given as,

$$B^f_{\text{Stab}}(\{\mathbf{w}^f, q\}, \{\mathbf{v}^f, p\}) = \sum_{e=1}^{nel} \int_{\Omega^{f^e}} \frac{1}{\rho^f} [\tau_{\text{SUPG}} \, \rho^f \, \mathbf{v}^f \cdot \nabla \mathbf{w}^f + \tau_{\text{PSPG}} \, \nabla q] \cdot \mathbf{r}_{\text{M}} \, d\Omega^f + \sum_{e=1}^{nel} \int_{\Omega^{f^e}} \tau_{\text{LSIC}} \, \rho^f \, (\nabla \cdot \mathbf{w}^f) \, (\nabla \cdot \mathbf{v}^f) \, d\Omega^f \, , \tag{12}$$

where $\mathbf{r}_{\text{M}}$ is the residual of the momentum equation and is given as

$$\mathbf{r}_{\text{M}} = \rho^f \, \frac{\partial \mathbf{v}^f}{\partial t} + \rho^f (\mathbf{v}^f \cdot \nabla \mathbf{v}^f) - \nabla \cdot \boldsymbol{\sigma}^f - \mathbf{g}^f \, . \tag{13}$$

Following [23–25], the stabilisation parameters τ_{SUPG}, τ_{PSPG} and τ_{LSIC} are defined as

$$\tau_{\text{SUPG}} = \left(\mathbf{v}^f \cdot \mathbf{G} \mathbf{v}^f + C_I \, \nu^2 \, \mathbf{G} : \mathbf{G} \right)^{-1/2} \tag{14}$$

$$\tau_{\text{PSPG}} = \tau_{\text{SUPG}} \tag{15}$$

$$\tau_{\text{LSIC}} = \left(\text{tr}\mathbf{G} \; \tau_{\text{SUPG}} \right)^{-1} \, , \tag{16}$$

where, C_I is a positive constant, independent of the mesh size, derived from an appropriate element-wise inverse estimate, and $\mathbf{G}$ is the element contravariant metric tensor. In this work, we take $C_I = 7$ for 2D problems and $C_I = 10$ for 3D problems. For cut cells, $\mathbf{G}$ is scaled based on the area/volume of the corresponding cell.

2.3.3. Nitsche's method

The terms corresponding to the Nitsche's method are given as,

$$B^f_{\text{Nitsche}}(\{\mathbf{w}^f, q\}, \{\mathbf{v}^f, p\}) = \gamma_{\text{N}_1} \int_{\Gamma_{\text{D}}} \mathbf{w}^f \cdot (\mathbf{v}^f - \hat{\mathbf{v}}) \, d\Gamma_{\text{D}} - \int_{\Gamma_{\text{D}}} \mathbf{w}^f \cdot (\boldsymbol{\sigma}(\{\mathbf{v}^f, p\}) \cdot \mathbf{n}^f) \, d\Gamma_{\text{D}} - \gamma_{\text{N}_2} \int_{\Gamma_{\text{D}}} (\boldsymbol{\sigma}(\{\mathbf{w}^f, q\}) \cdot \mathbf{n}^f) \cdot (\mathbf{v}^f - \hat{\mathbf{v}}) \, d\Gamma_{\text{D}} \, , \tag{17}$$

where, $\gamma_{\mathrm{N}_1} \geq 0$ is a penalty parameter and the choice of $\gamma_{\mathrm{N}_2} = 1$ results in symmetric Nitsche method while $\gamma_{\mathrm{N}_2} = -1$ results in unsymmetric Nitsche method. The boundary Γ_{D} is the union of boundaries of fluid grid where Dirichlet boundary conditions are applied and fluid-solid interfaces, i.e., $\Gamma_{\mathrm{D}} = \Gamma^f_{\mathrm{D}} \bigcup \Gamma^{f-s}$. Therefore, $\hat{\mathbf{v}} = \bar{\mathbf{v}}^f$ on Γ^f_{D} and $\hat{\mathbf{v}} = \mathbf{v}^s$ on Γ^{f-s}. The penalty parameter is computed using the following empirical formula.

$$\gamma_{N_1} = \begin{cases} \frac{a^2}{\max(h_x, h_y)} & \text{for 2D} \\ \frac{a^2}{\max(h_x, h_y, h_z)} & \text{for 3D} \end{cases} \tag{18}$$

where, a is the order of the b-spline basis, and h_x, h_y and h_z are the lengths of an element at the base level of the background mesh. This empirical formula has been obtained by performing local eigenvalue analysis of background grid elements without immersed solids. For $h_x = h_y = h_z$, the value of γ_{N_1} computed using the above formula is equal to the one obtained from the local eigenvalue problem. Even though the penalty parameter computed using the above formula is smaller than its analytical value for a fluid element cut by the immersed solid, in our experience, it provides a sufficient stablisation for the unsymmetric Nitsche method when applied to fluid-flexible structure interaction problems.

2.3.4. Cut cell stabilisation

It is now an established fact that the presence of small cut cells leads to system matrices with large condition numbers and sub-optimal convergence rates. In order to overcome this issue, we have employed the ghost-penalty operators in the present framework, see [20, 21], and references therein, for a comprehensive study of the performance of ghost penalty terms in the context of b-spline grids. These ghost-penalty terms enforce a suitable amount of continuity across the boundaries between cut cells and the active cells in the interior of the physical domain. In this work, we apply ghost-penalty operators only on the boundaries of cut-cells, as shown schematically in Fig. 1.

The ghost penalty terms for the incompressible Navier-Stokes equations with velocity $\mathbf{v}^f$ and pressure p as independent variables are defined as,

$$\mathcal{B}^f_{\mathrm{GP}}(\{\mathbf{w}^f, q)\}, \{(\mathbf{v}^f, p)\}) = \gamma^u_{\mathrm{GP}}\, \mu\, \mathcal{G}_1(\mathbf{w}^f, \mathbf{v}^f) + \gamma^p_{\mathrm{GP}}\, \frac{1}{\mu} g_3(q, p)\,, \tag{19}$$

where,

$$\mathcal{G}_1(\mathbf{w}, \mathbf{v}) := \sum_{i=1}^{d} \sum_{F \in \mathcal{F}} h^{2a-1} \int_F [D^a w_i][D^a v_i]\, dF \tag{20}$$

$$g_3(w, v) := \sum_{F \in \mathcal{F}} h^{2a+1} \int_F [D^a w][D^a v]\, dF\,. \tag{21}$$

where, $[D^j(\bullet)]$ denotes the jump of the normal derivative of $(\bullet)$ of order j on the face F, a is the order of the b-spline basis function, h is element length scale of face F, and γ^u_{GP} and γ^p_{GP} are the dimensionless ghost penalty parameters for

velocity and pressure, respectively. γ^u_{GP} and γ^p_{GP} can typically be chosen within a wide range of values spanning several orders of magnitude, such that they are small enough not to jeopardise accuracy but sufficiently large to effectively avoid excessive matrix condition numbers.

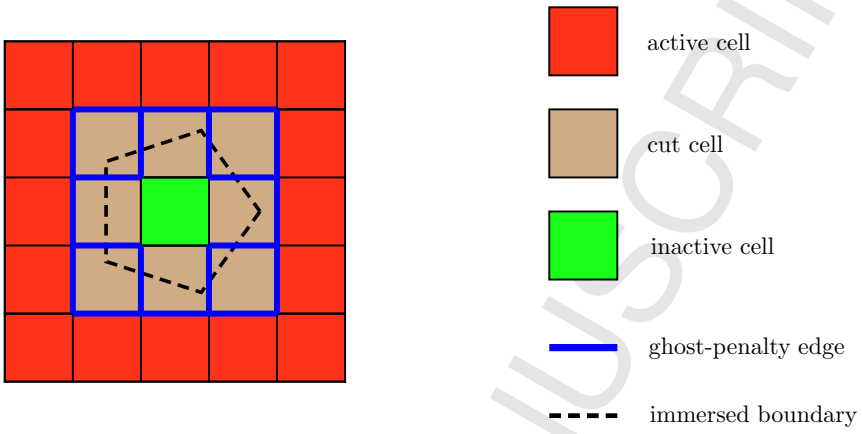

Figure 1: Active, inactive and cut cells for a typical scenario. Ghost penalty operators are applied only on the edges of the background grid highlighted in blue color.

2.3.5. Integration of cut cells

In the present framework, we have implemented two techniques for the purpose of integration of cut cells: (i) sub-triangulation, in which the active portion of the cell is subdivided into triangles and the quadrature points from the triangles are used to integrate the cut cells, and (ii) adaptive integration, which is based on the simple uniform subdivision of cut cells. These two techniques are demonstrated using a simple problem in Fig. 2. Each of these techniques has its relative advantages and disadvantages. While sub-triangulation can result in the accurate integration of cut-cells with fewer quadrature points, adaptive integration requires a large number of quadrature points in order to obtain meaningful results. Nonetheless, sub-triangulation poses serious limitations on the nature of representation of the immersed boundary, in the majority of the cases restricting the boundary to be represented (or approximated) by straight edges. On the other hand, adaptive integration poses no such restrictions on the description of the boundary. Adaptive integration is useful especially for 3D problems due to the fact that tetrahedralisation is much more complicated than triangulation. An efficient adaptive integration procedure is presented in Dettmer et al. [20].

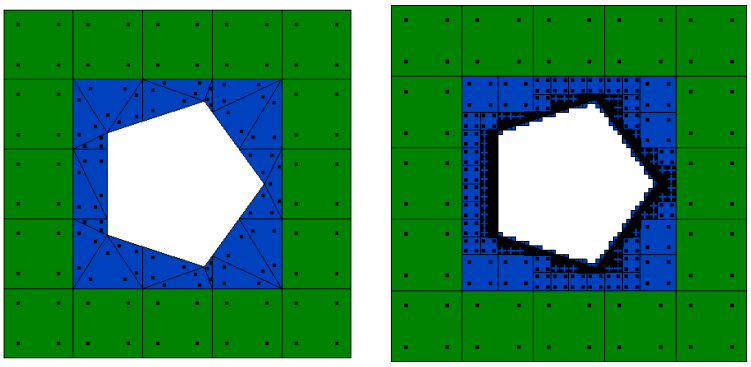

(a) Sub-triangulation (b) Adaptive integration

Figure 2: Integration of cut cells using sub-triangulation and adaptive integration.

2.4. Finite element formulation for the solid problem

In the present work, we use the standard linear Lagrange polynomials with the F-bar formulation of de Souza Neto et al. [27] for modelling the deformation behaviour of flexible solids. As this finite element formulation for the solid problem is well established, we refer the reader to [27, 28] for the discussions on the F-bar formulation.

2.4.1. Contact formulation

In this work, contact between solids is modelled using the standard node-to-segment contact elements with Lagrange multipliers to impose the contact constraints. We point out that the proposed immersed framework does not impose any limitations on the choice of contact formulation, and could be extended without any conceptual difficulties to include the standard penalty formulation, various forms of purely Lagrangian and augmented-Lagrangian approach, or the recent Nitsche based methodologies. Simple Lagrange multipliers based contact formulation that is used in this work is ideally suited for a relatively simple applications of interest discussed here involving check valves, in which a deforming solid interacts with rigid solid(s). This is designed primarily to demonstrate the feasibility of the proposed immersed framework to handle the fluid-structure interaction problems involving solid-to-solid contact. As this contact modelling technique is already well-established in the literature on computational contact mechanics, we refer the reader to Zienkiewicz and Taylor [29] and Wriggers [30] for comprehensive details on the topic.

Contacts between solids are resolved during the solution of the solid sub-system by solving the resulting non-linear problem using the classical Newton-Raphson scheme. As a staggered scheme is used for resolving the fluid-solid coupling, the overall computational cost of contact modelling in the present work is negligible. This is due to the fact that the contact modelling does not interfere with the solution of the fluid sub-system. Also, as the flexible solids are modelled using finite strain formulation, the solid sub-system is already non-linear and, therefore, is solved using the Newton-Raphson scheme.

3. Fluid-solid coupling

Efficient resolution of fluid-solid coupling is an important aspect of numerical schemes for FSI since the way fluid-solid coupling is resolved significantly affects the robustness, accuracy and efficiency of a numerical scheme for FSI. In literature, numerous techniques are available for resolving the fluid-solid coupling, with each method having its relative advantages and disadvantages. Among these techniques Dirichlet-Neumann coupling is the most widely used, see [2, 3, 5, 6, 19, 31–41]. In this work, we use the staggered solution scheme based on Dirichlet-Neumann coupling proposed by Dettmer and Perić [6] that is proven to be second-order accurate. For the purpose of clarity and completeness, the pseudocode for the staggered scheme is illustrated in Algorithm 1. Here, $\beta \in (0, 1)$ is a user-defined parameter and will be referred to as the *relaxation factor* in the rest of the paper. Problems which feature strong added-mass effects require a small value of β. However, for smaller values of β, the truncation error becomes higher, thus requiring an increased number of time steps to retain the accuracy. Nonetheless, the amount of added-mass in the examples selected in the present article is moderate, hence the chosen value of β does not affect accuracy significantly. As demonstrated with the numerical examples, accurate numerical results are obtained without having to use excessive number of time steps.

For every time step:

Step 1: predict force on the solid: $\mathbf{F}^{s^P}_{n+1} = 2\,\mathbf{F}_n - \mathbf{F}_{n-1}$
Step 2: solve the solid problem for $\mathbf{d}^s_{n+1}$ and $\mathbf{v}^s_{n+1}$ using $\mathbf{F}^{s^P}_{n+1}$
Step 3: reposition immersed solid, activate/deactivate fluid degrees of freedom, update cut cell data
Step 4: solve the fluid problem to obtain force $\mathbf{F}^f_{n+1}$
Step 5: average the interface force: $\mathbf{F}_{n+1} = -\beta\,\mathbf{F}^f_{n+1} + (1-\beta)\,\mathbf{F}^{s^P}_{n+1}$
Step 6: proceed to next time step

Algorithm 1: Staggered scheme applied to the present immersed methodology.

3.1. Force transfer from fluid to solid

The force on the immersed solids due to the surrounding fluid is computed by performing the integration over its respective boundary. In the present framework, the boundary of the immersed solid matches exactly with the boundary on which interface conditions are applied on the fluid grid. Therefore, there is no loss of force/momentum when computing the force on the solid.

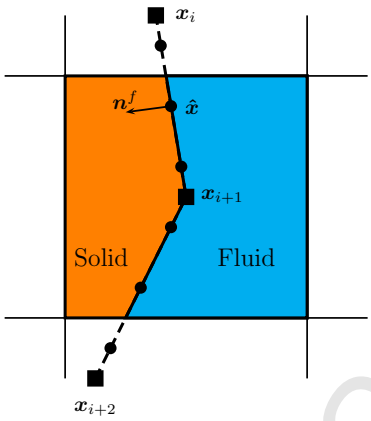

Figure 3: Computation of force vector on the solid mesh. Square dots denote the nodes on the boundary of the solid mesh and circular dots represent quadrature points.

The vector of forces on the j-th node of the solid mesh is computed as,

$$\mathbf{F}_j = \sum_{e=0}^{nedge} \sum_{i=0}^{nqp} N_{b,j}(\hat{\boldsymbol{x}})\, \mathbf{t}(\hat{\boldsymbol{x}})\, W_i J_i \tag{22}$$

where, $nedge$ is the number of boundary edges along the immersed solid, nqp is the number of quadrature points per each edge, W_i is weight of the quadrature point, J_i is the determinant of the Jacobian at the quadrature point, $N_{b,j}$ is the j-th basis function of the solid mesh and $\hat{\boldsymbol{x}}$ is the position vector at the quadrature point on the immersed edge. For an immersed edge discretised with n points $(\boldsymbol{x}_i, \ldots, \boldsymbol{x}_{i+n})$, the position vector $\hat{\boldsymbol{x}}$ is computed using the interpolation relation

$$\hat{\boldsymbol{x}} = \sum_{k=0}^{n} N_{b,k} \boldsymbol{x}_k \tag{23}$$

and the traction vector $\mathbf{t}(\hat{\boldsymbol{x}})$ is computed as,

$$\mathbf{t}(\hat{\boldsymbol{x}}) = \gamma_{\mathrm{N}_1} \left(\mathbf{v}^s - \mathbf{v}^f(\hat{\boldsymbol{x}})\right) + \boldsymbol{\sigma}^f(\hat{\boldsymbol{x}}) \cdot \mathbf{n}^f(\hat{\boldsymbol{x}}) \tag{24}$$

3.2. The issue of uncovering fluid DOFs

Whenever the interface moves into an element that was not part of the fluid domain during the previous time step all the DOFs corresponding to that element become active at the current time step. This leads to problems in evaluating acceleration at the current time step which might cause the simulation to terminate when large time steps are used. For fluid-rigid body interaction problems [21] we did not use any special techniques for treating uncovering of elements during FSI simulation. For such DOFs, we chose the value available from the last time instant they were active as the value for the previous time step. As the time steps selected were small, we have not observed any problems associated

with the uncovering of the elements. However, for the sake of completeness, we have implemented a simple mapping technique that does not require any matrix inversions, and is based on the assumption that the fictitious fluid inside the solid domain moves at the same velocity as that of the solid domain. The pseudocode for the mapping technique is described in Algorithm 2. This technique is applied between Step 3 and Step 4 of the staggered scheme described in Algorithm 1 in Section 3. In this way, the fluid velocity DOFs that are completely inside the solid domain, and hence, inactive in the current fluid domain, get the information from the solid velocity; and those that belong to the cut cells get the velocity information once the fluid problem is solved at Step 4. As illustrated in Fig. 4, this technique provides significantly better solution information for inactive DOFs at the current time step without having to spend a significant amount of computational resources.

For every solid node i:

1. get the nodal position $\mathbf{x}^s_{n+1,i}$ and velocity $\mathbf{v}^s_{n+1,i}$
2. find the fluid cell in which the node i lies
3. find the basis functions of the fluid grid that are active at the spatial location $\mathbf{x}^s_{n+1,i}$
4. replace the values of the velocity degrees of freedom of these active basis functions of the fluid grid with the velocity of the solid node, $\mathbf{v}^s_{n+1,i}$
5. proceed to next node

Algorithm 2: Pseudocode for the mapping technique used for *uncovering*.

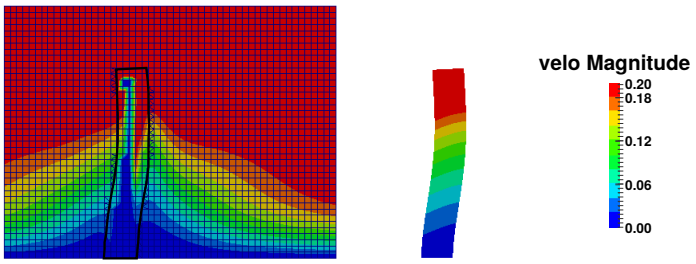

(a) solution obtained without the mapping technique

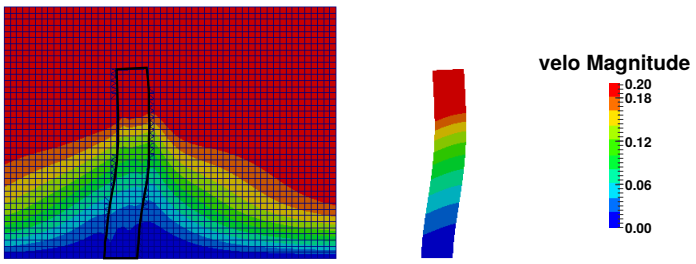

(b) solution obtained with the mapping technique

Figure 4: Thick beam in cross flow: the effect of the mapping technique on *uncovering* for fluid DOFs.

4. Numerical examples

The performance of the proposed scheme in terms of its accuracy and robustness is assessed by studying a number of numerical simulations. The following problems are studied:

(i) cross-flow over a thick flexible beam

(ii) oscillating beam model by Turek and Hron [32],

(iii) flutter of a bridge deck, and

(iv) check valve with flexible plate.

For all the examples presented in this paper (a) unsymmetric Nitsche method is used for imposing boundary as well as interface conditions, (b) the ghost penalty parameters are $\gamma_{\text{GP}_u} = \gamma_{\text{GP}_p} = 0.01$, unless otherwise specified, (c) the solid is discretised with linear Lagrange elements modelled with F-bar formulation and (d) the spectral radii values for generalised-α schemes for the fluid and solid solvers are $\rho^f_\infty = \rho^s_\infty = 0.0$.

4.1. Thick beam in cross flow

The geometry and boundary conditions of the problem, adopted from [42], are shown in Fig. 5. The density of the fluid is $\rho^f = 1.0$ and its dynamic viscosity is $\mu^f = 0.01$. The beam is modelled with Neo-Hookean material with density $\rho^s = 1.0$, Young's modulus $E^s = 200.0$ and Poisson's ratio $\nu^s = 0.3$. A time-invariant parabolic velocity profile $v_{in} = \frac{20}{6} y(0.6 - y)$ is imposed on the inlet.

Spatial and temporal convergence studies are performed on the hierarchical mesh shown in Fig. 6. The beam is discretised with 10×30 mesh. For each spatial discretisation, numerical results are obtained with three different time steps, $\Delta t = \{0.04, 0.02, 0.01\}$. A constant relaxation parameter $\beta = 0.05$ is used for all the simulations. The horizontal displacement of point A at $t = 5.0$ tabulated in Table. 1 indicate clear spatial and temporal convergence of the proposed scheme. The evolution of horizontal displacement of point A for a subset of the simulation cases is illustrated in Fig. 7 and the contour plots of fluid velocity magnitude and fluid pressure at the last time step of the simulation with the Level-2 linear b-spline (Q_1) mesh and $\Delta t = 0.01$ are shown in Fig. 8.

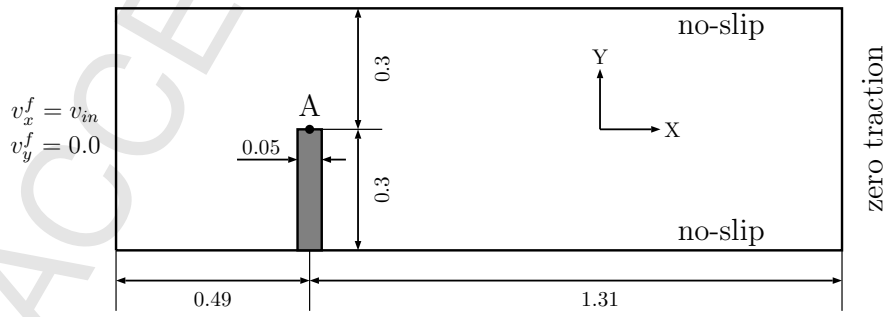

Figure 5: Thick beam in cross flow: geometry and boundary conditions.

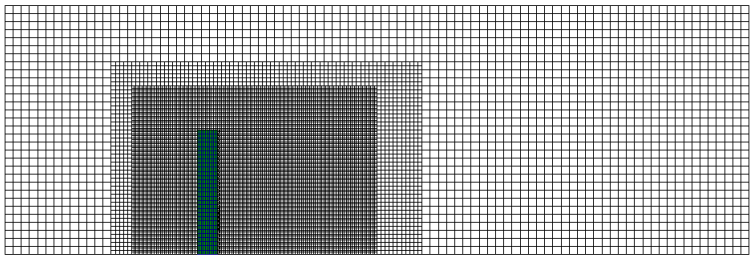

Figure 6: Thick beam in cross flow: hierarchical b-spline mesh used for the simulation.

	Level-1		Level-2	
	linear(Q_1)	quadratic(Q_2)	linear(Q_1)	quadratic(Q_2)
Total DOFs	16689	17085	38034	38397
$\Delta t = 0.04$	0.1239	0.1305	0.1285	0.1292
$\Delta t = 0.02$	0.1249	0.1304	0.1284	0.1292
$\Delta t = 0.01$	0.1248	0.1304	0.1284	0.1292

Table 1: Thick beam in cross flow: horizontal displacement of point A at $t = 5.0$. Total DOFs reported are at the beginning of the simulation and they remain approximately the same, for each discretisation, during the whole simulation.

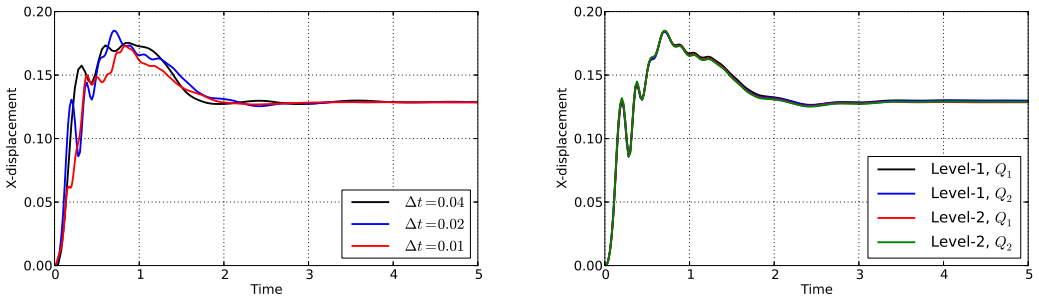

(a) Level-2 with linear(Q_1) b-splines

(b) $\Delta t = 0.02$

Figure 7: Thick beam in cross flow: horizontal displacement of point A.

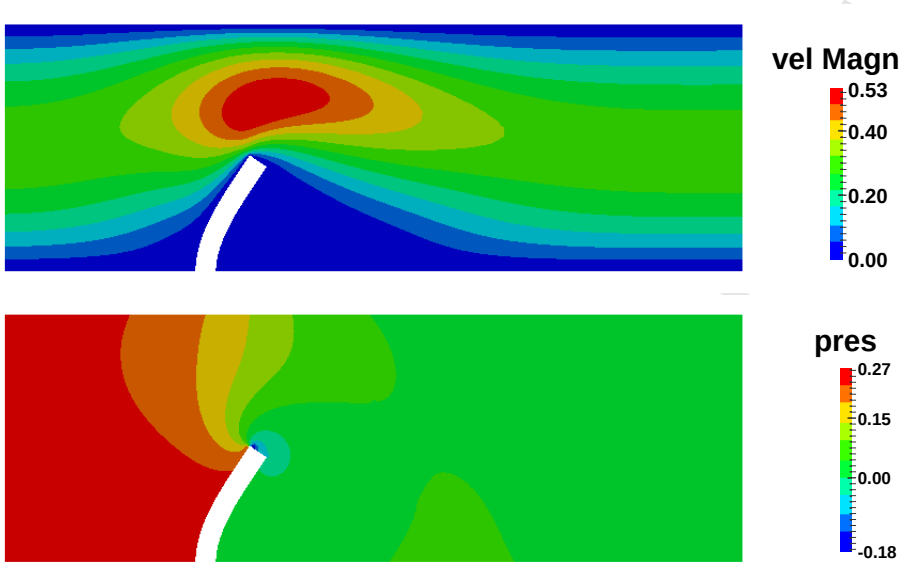

Figure 8: Vertical beam: contour plots of velocity magnitude and pressure at $t = 5.0$ obtained with Level-2 Q_1 b-splines and $\Delta t = 0.01$.

4.2. Turek benchmark problem

This problem, introduced by Turek and Hron [32], is widely used as a benchmark example to test the numerical schemes for fluid-flexible solid interaction. The geometry and boundary conditions of the problem are shown in Fig. 9(a). The physics of the problem is such that vortices start developing due to the asymmetry in the geometry which cause the beam to oscillate. Once the vortices are fully developed, the beam will undergo periodic oscillations in its second harmonic mode. In this example we consider the test case **FSI2** from [32], for which fluid density and viscosity are $\rho^f = 10^3$ and $\mu^f = 1$, respectively; and solid density, Young's modulus and Poisson's ratio, respectively, are $\rho^s = 10^4$, $E = 1.4 \times 10^6$ and $\nu^s = 0.4$. The beam is modelled with Saint Venant-Kirchhoff material model. A parabolic velocity profile $v_{in} = \frac{6}{0.1681} y(0.41 - y)$ is applied at the inlet. The inlet velocity is increased sinusoidally to v_{in} in the time interval $[0, 2]$ and then kept constant at v_{in} for the rest of the simulation.

A hierarchical b-spline mesh shown in Fig. 9(b) is used with linear (Q_1) and quadratic (Q_2) b-splines. The beam is discretised with 200×10 linear quadrilateral elements. The relaxation parameter is set to $\beta = 0.1$. Simulations are performed with two different time steps, $\Delta t = 0.002$ and $\Delta t = 0.001$. The amplitude and the frequency of the oscillation of the vertical displacement of point A obtained for all the simulations are tabulated in Table. 2. These values indicate that the results obtained with the present scheme converge to the reference values as the discretisation and time step is refined. Evolution of the vertical displacement of point A obtained with Level-3 mesh and $\Delta t = 0.001$ is displayed in Fig. 10. Typical contour plots of pressure and velocity magnitude at two time instants are presented in Figs. 12 and 11, respectively.

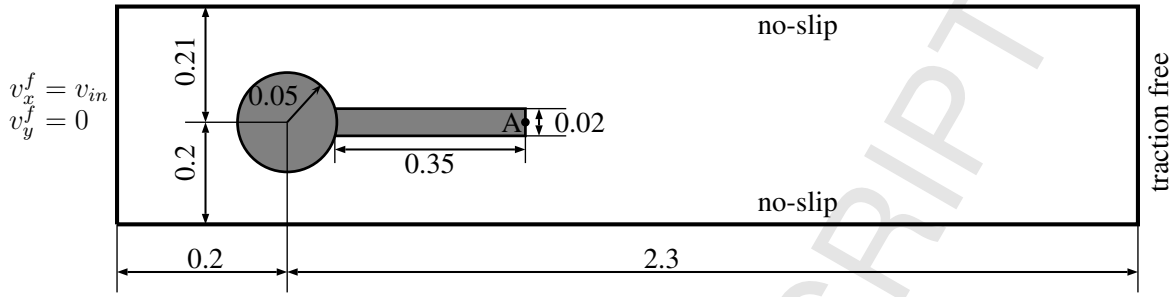

(a) Geometry and boundary conditions (not to scale).

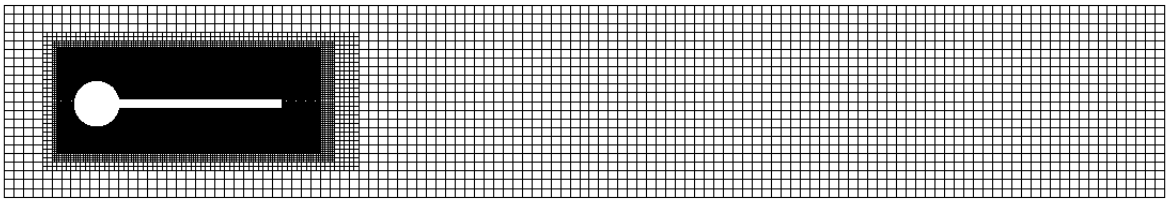

(b) Hierarchical b-spline mesh for the fluid.

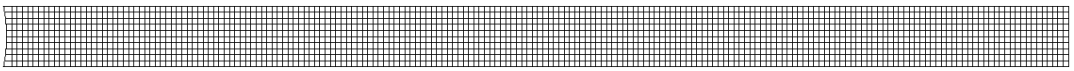

(c) Solid mesh for the beam.

Figure 9: Turek benchmark problem: geometry, boundary conditions and spatial discretisations of the fluid and solid.

	DOF	$\max(d_y^s \times 10^3)$	f_o
Turek and Hron [32] - Level-2, $\Delta t = 0.001$	19488	1.18 ± 78.80	2.00
Turek and Hron [32] - Level-3, $\Delta t = 0.001$	76672	1.25 ± 79.30	2.00
Turek and Hron [32] - Level-4, $\Delta t = 0.001$	304128	1.23 ± 80.60	2.00
Present - Level-2, Q_1, $\Delta t = 0.002$	≈ 26000	1.13 ± 73.33	2.00
Present - Level-2, Q_2, $\Delta t = 0.002$	≈ 26000	1.21 ± 75.42	2.00
Present - Level-3, Q_1, $\Delta t = 0.002$	≈ 70000	1.28 ± 75.37	2.00
Present - Level-3, Q_2, $\Delta t = 0.002$	≈ 70000	1.23 ± 76.80	2.00
Present - Level-2, Q_1, $\Delta t = 0.001$	≈ 26000	1.39 ± 75.92	2.00
Present - Level-2, Q_2, $\Delta t = 0.001$	≈ 26000	1.25 ± 78.27	2.00
Present - Level-3, Q_1, $\Delta t = 0.001$	≈ 70000	1.25 ± 78.32	2.00
Present - Level-3, Q_2, $\Delta t = 0.001$	≈ 70000	1.22 ± 79.85	2.00

Table 2: Turek beam: summary of vertical displacement of point A (d_y^s) and frequency of oscillations (f_o).

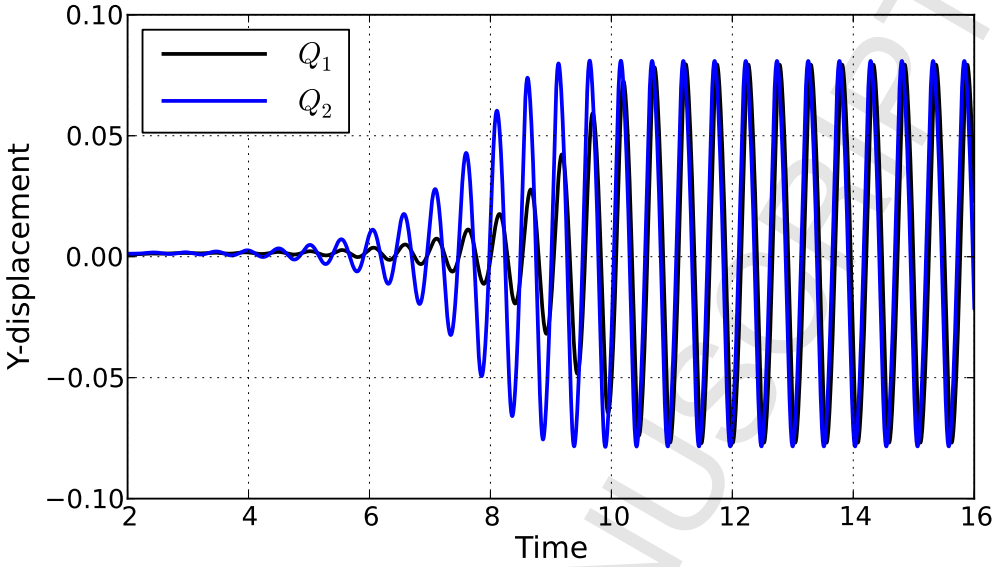

Figure 10: Turek benchmark problem: vertical displacement of point A obtained with Level-3 mesh and $\Delta t = 0.001$.

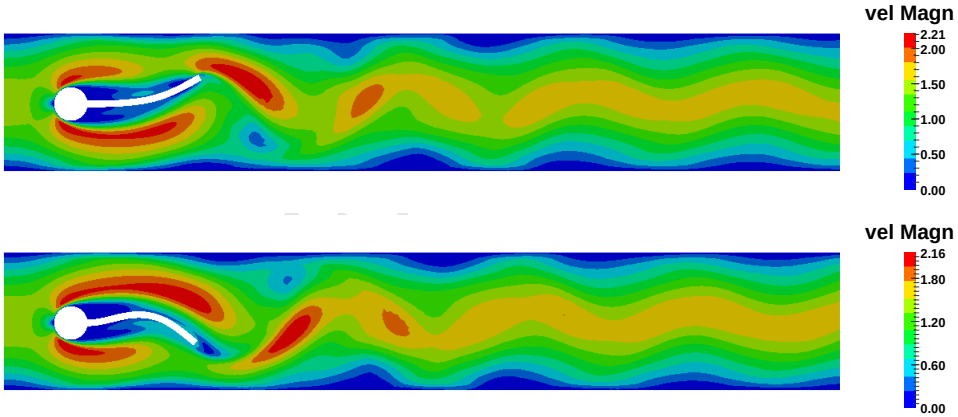

Figure 11: Turek benchmark problem: contour plots of velocity magnitude.

Figure 12: Turek benchmark problem: contour plots of pressure.

4.3. Flutter of an elastic bridge

This example is concerned with the flutter of an elastic bridge. Flutter is a dynamic instability of an elastic structure subjected to fluid flow. This example represents a simplified model of the famous Tacoma Narrows bridge which collapsed eventually after undergoing violent vibrations. This problem has been previously studied by Dettmer and Perić [6] using body-fitted ALE approach and the staggered scheme used in the present work. The geometry and boundary conditions of the problem are shown in Fig. 13(a). The bridge is of size $1 \times 4 \times 30$ and clamped at its both ends. The density and viscosity of the fluid are $\rho^f = 1.0$ and $\mu^f = 0.01$, respectively. The properties of the bridge material are: density $\rho^s = 70.6$, shear modulus $\mu^s = 823.2$ and bulk modulus $\kappa^s = 1783.6$; and it material model used is Neo-Hookean. Based on the inflow velocity of $v_{in} = 2.5$ and the thickness of the bridge, the Reynolds number is $Re = 250$.

The hierarchical mesh shown in Fig. 13(b), with linear b-splines, is used for the simulation. The fluid mesh consists of 171212 DOFs at the first step of the simulation, and the beam is discretised with $3 \times 2 \times 10$ linear hexahedral elements. Three levels of adaptive integration are used for the integration of cut cells. The relaxation parameter for the staggered scheme is $\beta = 0.5$. The ghost-penalty parameters are $\gamma^u_{\text{GP}} = \gamma^p_{\text{GP}} = 0.0001$. The inlet velocity is ramped smoothly during first ten time units and then kept constant at v_{in}. A constant time step of $\Delta t = 0.5$ is used. The evolution of vertical displacement of the midpoint of the leading edge of the bridge is presented in Fig. 14, along with the value obtained with the body-fitted ALE approach proposed in [6]. This graph shows that the solution obtained with the present scheme is, in terms of frequencies and amplitudes, in agreement with the solution obtained in [6]. Differences are attributed to the relatively coarse discretisations in both simulations. Typical contour plots of fluid pressure and streamlines, along with the deformed configuration of the beam, at two time instants are shown in Figs. 15 and 16, respectively.

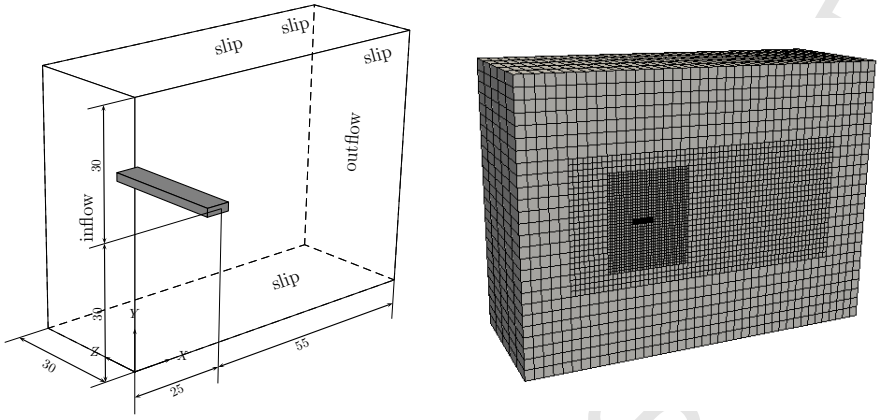

(a) (b)

Figure 13: Bridge flutter: (a) geometry and boundary conditions and (b) hierarchical mesh used for the analysis.

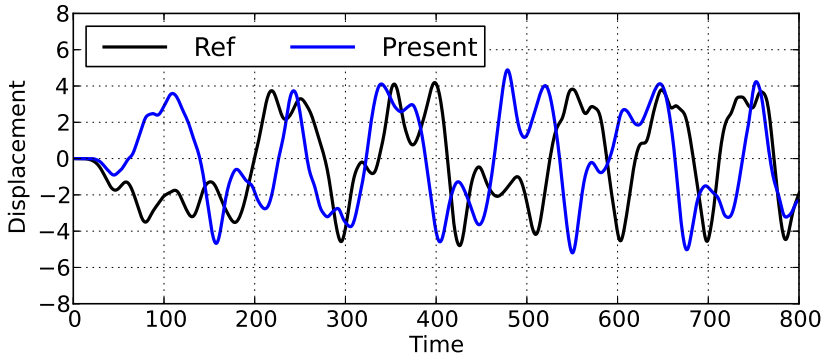

Figure 14: Bridge flutter: vertical displacement of the midpoint of the leading edge.

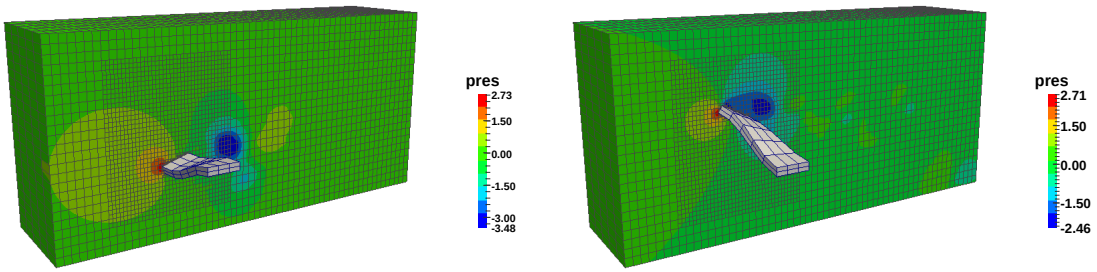

(a) $t = 555$ (b) $t = 750$

Figure 15: Bridge flutter: contour plots of pressure in the refined portion of the fluid grid.

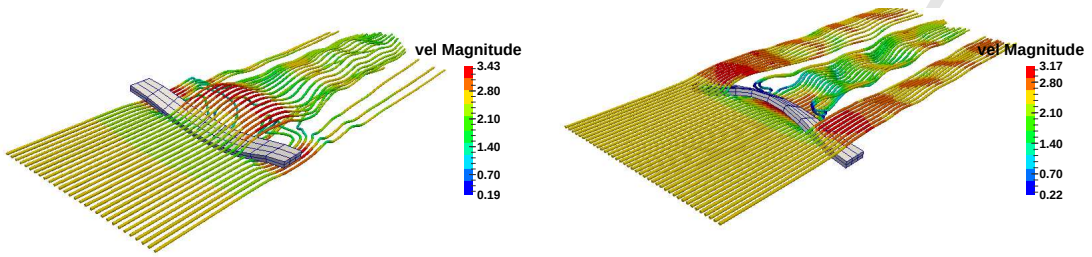

(a) $t = 555$ (b) $t = 750$

Figure 16: Bridge flutter: streamlines and the deformed configuration of the beam.

4.4. Check valve with elastic plate

In this example, we apply the proposed numerical methodology to simulate the fluid-structure interaction in a check valve in which the valve plate is modelled as a flexible solid. This example demonstrates the applicability of the proposed framework for problems consisting of complex geometries and evolving solid-solid contacts. The geometry and boundary conditions of the problem are shown in Fig. 17(a). The density and viscosity of the fluid are $\rho^f = 800.0$ kg/m^3 and $\mu^f = 500$ cP, respectively. The beam is of thickness 0.25 mm and is modelled with Neo-Hookean material with density $\rho^s = 8000$ kg/m^3, Young's modulus $E^s = 1.0$ GPa and Poisson's ratio $\nu^s = 0.3$. The contact between the bottom surface of beam and valve's seat is modelling as a frictionless normal contact using Lagrange multipliers.

Simulations are performed on the hierarchical mesh shown in Fig. 17(b). With linear b-splines the fluid mesh consists of 88416 DOFs at the first time step of the simulation. Integration of cut cells is performed using four levels of adaptive integration. The relaxation parameter for the staggered scheme is $\beta = 0.05$. The inlet pressure is varied sinusoidally with a frequency of 10 Hz; and a constant time step of $\Delta t = 1.0$ ms is used. The vertical displacement of the tip of the beam, total contact force and flow rate are displayed in Fig. 18, along with the input pressure profile. These graphs illustrate that the closing of the valve when the flow is reveresed during the suction part of the pressure cycle is captured well. The direct consequence of this can be observed in *zero flow rate* during the suction part. Contour plots of velocity mangitude and pressure when the valve is its highest opening position are shown in Fig. 19.

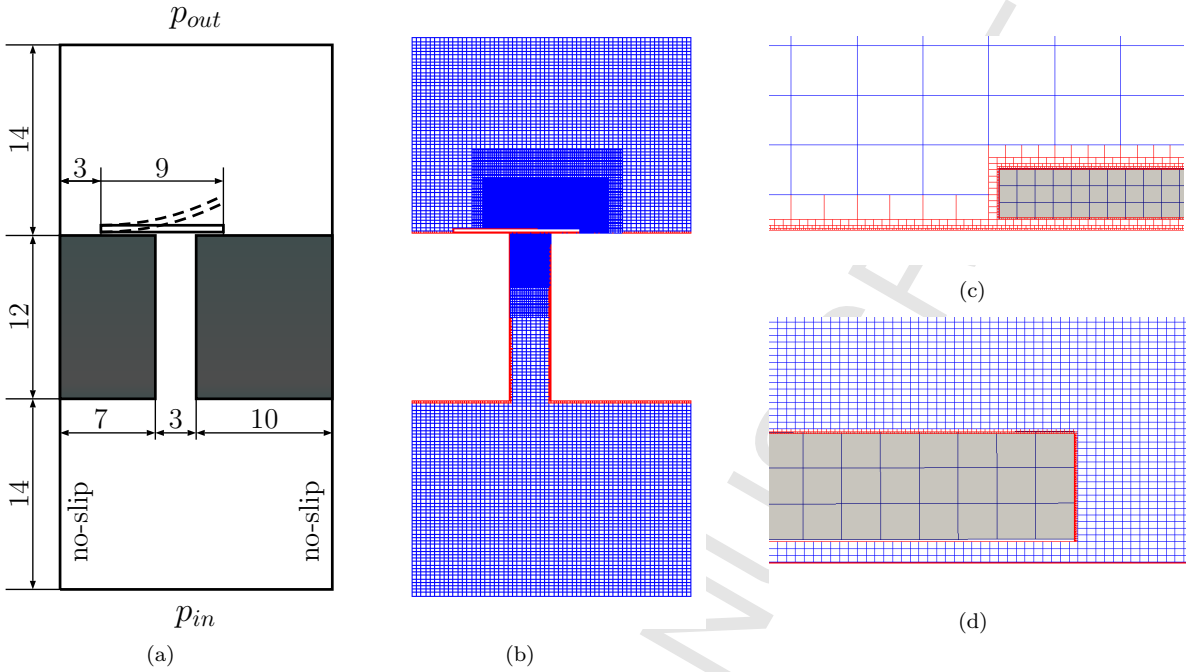

Figure 17: Check valve with elastic plate: (a) geometry and boundary conditions, (b) hierarchical mesh used for the analysis, (c) discretisation around the left end of the beam and (d) discretisation around the right end of the beam. Cells shown in red color are for the adaptive integration.

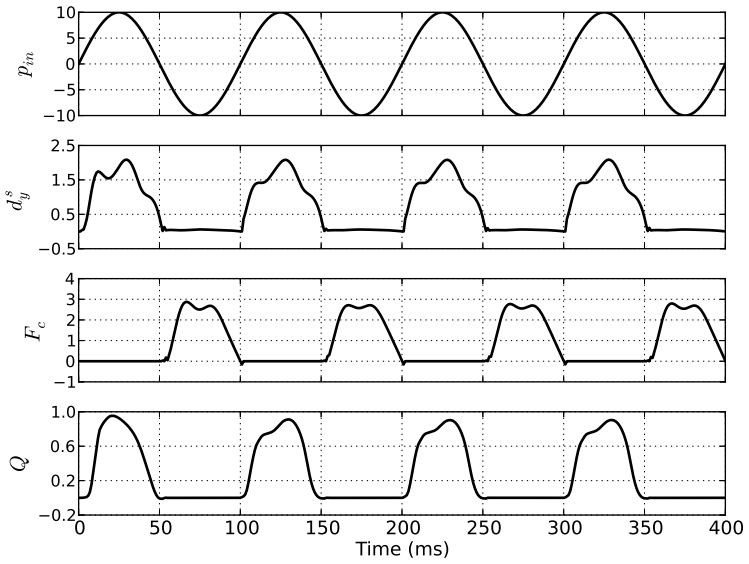

Figure 18: Check valve with elastic plate: response diagram - input pressure $p_{in} = 10\ \sin(2\pi t/100)$ [bar], tip displacement d_y^s [mm], total contact force F_c [N] and flow rate Q [ml/ms].

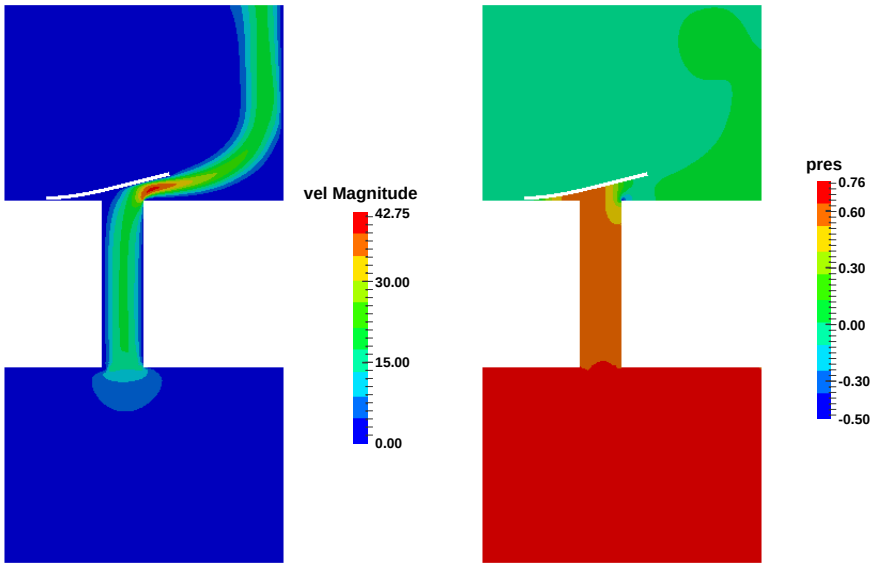

(a) (b)

Figure 19: Check valve with elastic plate: contour plots of velocity magnitude and pressure when the valve is in its highest opening position.

5. Summary and conclusions

We have presented a robust and efficient numerical framework for the simulation of fluid-structure interaction involving laminar viscous incompressible fluid, flexible solids and solid-solid contact. The promising feature of the proposed framework is the efficiency resulting from the use of the staggered scheme in which fluid and solid sub-problems are solved *only once* during a time step. Moreover, computationally efficient fluid grids that yield accurate numerical results can be generated by exploiting the hierarchical property of b-splines.

The proposed scheme is applied to several benchmark examples. Spatial and temporal convergence studies of the scheme are assessed by the studying the problems of cross flow over a flexible beam and vortex-induced oscillations of a flexible beam. As demonstrated with the numerical examples, the results obtained with the proposed scheme are in good agreement with reference values. Key advantages of the proposed methodology lie in the robustness and the efficiency of the staggered scheme and the effective utilisation of the hierarchical property of b-splines. The example of bridge flutter illustrates the robustness of the proposed scheme for three-dimensional problems where the solid undergoes extremely large deformations, and the example of check valve clearly demonstrates the applicability of the proposed scheme to complex industrial fluid-structure interaction problems involving solid-to-solid contacts. In conclusion, the present framework based on the immersed finite element methodology proposed in [20, 21] has been proven to be a robust and efficient numerical framework for the modelling of complex coupled fluid-structure interaction. The ongoing research effort focusses on extending the proposed framework to high-performance computing

architectures and its application to large-scale industrial simulations.

Acknowledgements

This research project is funded by Schaeffler Technologies AG & Co. KG, Germany. This support is gratefully acknowledged.

References

[1] A. A. Johnson and T. E. Tezduyar. Mesh update strategies in parallel finite element computations of flow problems with moving boundaries and interfaces. *Computer Methods in Applied Mechanics and Engineering*, 119:73–94, 1994.

[2] W. G. Dettmer and D. Perić. A computational framework for fluid-structure interaction: Finite element formulation and applications. *Computer Methods in Applied Mechanics and Engineering*, 195:5754–5779, 2006.

[3] W. G. Dettmer and D. Perić. A computational framework for fluid-rigid body interaction: Finite element formulation and applications. *Computer Methods in Applied Mechanics and Engineering*, 195:1633–1666, 2006.

[4] W. G. Dettmer and D. Perić. A computational framework for free surface fluid flows accounting for surface tension. *Computer Methods in Applied Mechanics and Engineering*, 195:3038–3071, 2006.

[5] W. G. Dettmer and D. Perić. A fully implicit computational strategy for strongly coupled fluid-solid interaction. *Archives of Computational Methods in Engineering*, 14:205–247, 2007.

[6] W. G. Dettmer and D. Perić. A new staggered scheme for fluid-structure interaction. *International Journal for Numerical Methods in Engineering*, 93:1–22, 2013.

[7] P. H. Saksono, W. G. Dettmer, and D. Perić. An adaptive remeshing strategy for flows with moving boundaries and fluid-structure interaction. *International Journal for Numerical Methods in Engineering*, 71:1009–1050, 2007.

[8] C. S. Peskin. The immersed boundary method. *Acta Numerica*, 11:479–517, 2002.

[9] L. Zhang, A. Gerstenherger, X. Wang, and W. K. Liu. Immersed finite element method. *Computer Methods in Applied Mechanics and Engineering*, 193:2051–2067, 2004.

[10] L. T. Zhang and M. Gay. Immersed finite element method for fluid-structure interactions. *Journal of Fluids and Structures*, 23:839–857, 2007.

[11] T. Rüberg and F. Cirak. Subdivision-stabilised immersed b-spline finite elements for moving boundary flows. *Computer Methods in Applied Mechanics and Engineering*, 209-212:266–283, 2012.

[12] T. Rüberg and F. Cirak. A fixed-grid b-spline finite element technique for fluid-structure interaction. *International Journal for Numerical Methods in Fluids*, 74:623–660, 2014.

[13] D. Kamensky, M. Hsu, D. Schillinger, J. A. Evans, A. Aggarwal, Y. Bazilevs, M. S. Sacks, and T. J. R. Hughes. An immersogeometric variational framework for fluid-structure interaction: application to bioprosthetic heart valves. *Computer Methods in Applied Mechanics and Engineering*, 284:1005–1053, 2015.

[14] F. Xu, D. Schillinger, D. Kamensky, V. Varduhn, C. Wang, and M. Hsu. The tetrahedral finite cell method for fluids: Immersogeometric analysis of turbulent flow around complex geometries. *Computers and Fluids*, 141:135–154, 2016.

[15] E. Burman and P. Hansbo. Fictitious domain methods using cut elements III. A stabilized Nitsche method for Stoke's problem. *ESAIM: Mathematical Modelling and Numerical Analysis*, 48:859–874, 2014.

[16] Y. Wang, P. K. Jimack, and M. A. Walkley. A one-field monolithic fictitious domain method for fluid-structure interactions. *Computer Methods in Applied Mechanics and Engineering*, 317:1146–1168, 2017.

[17] C. Kadapa, W. G. Dettmer, and D. Perić. NURBS based least-squares finite element methods for fluid and solid mechanics. *International Journal for Numerical Methods in Engineering*, 101:521–539, 2015.

[18] C. Kadapa, W. G. Dettmer, and D. Perić. Subdivision based mixed methods for isogeometric analysis of linear and nonlinear nearly incompressible materials. *Computer Methods in Applied Mechanics and Engineering*, 305:241–270, 2016.

[19] C. Kadapa, W. G. Dettmer, and D. Perić. A fictitious domain/distributed Lagrange multiplier based fluid-structure interaction scheme with hierarchical B-Spline grids. *Computer Methods in Applied Mechanics and Engineering*, 301:1–27, 2016.

[20] W. G. Dettmer, C. Kadapa, and D. Perić. A stabilised immersed boundary method on hierarchical b-spline grids. *Computer Methods in Applied Mechanics and Engineering*, 311:415–437, 2016.

[21] C. Kadapa, W. G. Dettmer, and D. Perić. A stabilised immersed boundary method on hierarchical b-spline grids for fluid-rigid body interaction with solid-solid contact. *Computer Methods in Applied Mechanics and Engineering*, 318:242–269, 2017.

[22] E. Burman, S. Claus, P. Hansbo, M. G. Larson, and A. Massing. CutFEM: Discretizing geometry and partial differential equations. *International Journal for Numerical Methods in Engineering*, 104:472–501, 2014.

[23] A. N. Brooks and T. J. R. Hughes. Streamline upwind/Petrov-Galerkin formulations for convection dominated flows with particular emphasis on the incompressible Navier-Stokes equations. *Computer Methods in Applied Mechanics and Engineering*, 32:199–259, 1982.

[24] T. J. R. Hughes, L. P. Franca, and M. Balestra. A new finite element formulation for computational fluid dynamics: V. Circumventing the Babuska-Brezzi condition: A stable Petrov-Galerkin formulation of the Stokes problem accommodating equal-order interpolations. *Computer Methods in Applied Mechanics and Engineering*, 59:85–99, 1986.

[25] T. E. Tezduyar, S. Mittal, S. E. Ray, and R. Shih. Incompressible flow computations with stabilized bilinear and linear equal-order-interpolation velocity-pressure elements. *Computer Methods in Applied Mechanics and Engineering*, 95:221–242, 1992.

[26] E. Burman. Ghost Penalty. *Comptes Rendus Mathematique*, 348:1217–1220, 2010.

[27] E. A. de Souza Neto, D. Perić, M. Dutko, and D. R. J. Owen. Design of simple low order finite elements for large strain analysis of nearly incompressible solids. *International Journal of Solids Structures*, 33:3277–3296, 1996.

[28] E. A. de Souza Neto, D. Perić, and D. R. J. Owen. *Computational Methods for Plasticity, Theory and Applications*. John Wiley and Sons, United Kingdom, 2008.

[29] O. C. Zienkiewicz and R. L. Taylor. *The Finite Element Method for Solid and Structural Mechanics*. Elsevier Butterworth and Heinemann, Oxford, England, Sixth edition, 2005.

[30] P. Wriggers. *Computational Contact Mechanics*. Springer, Berlin Heidelberg, 2006.

[31] W. A. Wall and E. Ramm. Fluid-structure interaction based upon a stabilized (ALE) finite element method. In *Idelsohn S. R., Onate E. (eds) Computational mechanics – new trends and applications, 4th World Congress on Computational Mechanics, CIMNE, Barcelona, Spain, Buenos Aires, Brazil.*, 1998.

[32] S. Turek and J. Hron. *Proposal for Numerical Benchmarking of Fluid-Structure Interaction between an Elastic Object and Laminar Incompressible Flow*, volume 53 - Fluid-Structure Interaction of *Lecture Notes in Computational Science and Engineering*, pages 371–385. Springer, Berlin, 2006.

[33] Y. Bazilevs, V. M. Calo, T. J. R. Hughes, and Y. Zhang. Isogeometric fluid-structure interaction: theory, algorithms, and computations. *Computational Mechanics*, 43:3–37, 2008.

[34] S. R. Idelsohn, F. Del Pin, R. Rossi, and E. Oñate. Fluid-structure interaction problems with strong added-mass effect. *International Journal for Numerical Methods in Engineering*, 80:1261–1294, 2009.

[35] M. Breuer, G. De Nayer, M. Münsch, Gallinger T., and R. Wüchner. Fluid-structure interaction using a partitioned semi-implicit predictor-corrector coupling scheme for the application of large-eddy simulation. *Journal of Fluids and Structures*, 29:107–130, 2012.

[36] S. Sicklinger, V. Belsky, B. Engelmann, H. Elmqvist, H. Olsson, R. Wüchner, and K. U. Bletzinger. Interface Jacobian-based Co-Simulation. *International Journal for Numerical Methods in Engineering*, 98:418–444, 2014.

[37] S. Sicklinger, D. Lerch, R. Wüchner, and K. U. Bletzinger. Fully coupled co-simulation of a wind turbine emergency brake maneuver. *Journal of Wind Engineering and Industrial Aerodynamics*, 144:134–145, 2015.

[38] J. W. Banks, W. D. Henshaw, and D. W. Schwendeman. An analysis of a new stable partitioned algorithm for FSI problems. Part I: Incompressible flow and elastic solids. *Journal of Computational Physics*, 269:108–137, 2014.

[39] J. W. Banks, W. D. Henshaw, and D. W. Schwendeman. An analysisof a new stable partitioned algorithm for FSI problems. Part II: Incompressible flow and structural shells. *Journal of Computational Physics*, 268:399–416, 2014.

[40] C. Förster, W. A. Wall, and E. Ramm. Artificial added mass instabilities in sequential staggered coupling of nonlinear structures and incompressible viscous flows. *Computer Methods in Applied Mechanics and Engineering*, 196:1278–1293, 2007.

[41] R. K. Jaiman, N. R. Pillalamarri, and M. Z. Guan. A stable second-order partitioned iterative scheme for freely vibrating low-mass bluff bodies in a uniform flow. *Computer Methods in Applied Mechanics and Engineering*, 301:187–215, 2016.

[42] S. Shahmiri. *A Hybrid ALE-Fixed-Grid Approach for Fluid-Structure Interaction*. PhD thesis, Technical University of Munich, Munich, Germany., 2014.